

Cite this article as: Zhao Yanchun, Jin Bo, Feng Yuanfei, et al. Effect of Co Content on Microstructure and Mechanical Properties of High-Entropy High-Temperature Shape Memory Alloy[J]. Rare Metal Materials and Engineering, 2025, 54(01): 10-16. DOI: 10.12442/j.issn.1002-185X.20240507.

ARTICLE

# Effect of Co Content on Microstructure and Mechanical Properties of High-Entropy High-Temperature Shape Memory Alloy

Zhao Yanchun<sup>1,2</sup>, Jin Bo<sup>1</sup>, Feng Yuanfei<sup>1</sup>, Ma Huwen<sup>1</sup>, Yu Zhiqi<sup>1</sup>, Feng Li<sup>1,2</sup>, Liaw Peter K<sup>3</sup>

<sup>1</sup>State Key Laboratory of Advanced Processing and Recycling of Nonferrous Metals, Lanzhou University of Technology, Lanzhou 730050, China; <sup>2</sup>Wenzhou Pump and Valve Engineering Research Institute of Lanzhou University of Technology, Wenzhou 325105, China; <sup>3</sup>Department of Materials Science and Engineering, University of Tennessee, Knoxville TN37996, USA

**Abstract:** (TiZrHf)<sub>50</sub>Ni<sub>30</sub>Cu<sub>20-x</sub>Co<sub>x</sub> (x=2, 4, 6, at%) high-entropy high-temperature shape memory alloys were fabricated by water-cooled copper crucible in a magnetic levitation vacuum melting furnace, and the effects of Co content on microstructure and mechanical properties were investigated. The results indicate that the grain size of the alloy decreases with increasing the Co content. In the as-cast state, the alloy consists primarily of the B19' phase, with a trace of B2 phase. The fracture morphology is predominantly composed of the B19' phase, whereas the B2 phase is nearly absent. Increasing the Co content or reducing the sample dimensions (*d*) markedly enhance the compressive strength and ductility of the alloy. When *d*=2 mm, the (TiZrHf)<sub>50</sub>Ni<sub>30</sub>Cu<sub>14</sub>Co<sub>6</sub> alloy demonstrates the optimal mechanical properties, achieving a compressive strength of 2142.39±1.8 MPa and a plasticity of 17.31±0.3%. The compressive cyclic test shows that with increasing the compressive strain, the residual strain of the (TiZrHf)<sub>50</sub>Ni<sub>30</sub>Cu<sub>14</sub>Co<sub>6</sub> alloy increases while the recovery ability declines. The superelastic recovery capability of the alloy is continuously enhanced. The superelastic recovery rate increases from 1.36% to 2.12%, the residual strain rate rises from 1.79% to 5.52%, the elastic recovery rate ascends from 3.86% to 7.36%, while the total recovery rate declines from 74.48% to 63.20%.

**Key words:** high-temperature shape memory alloy; high-entropy alloy; microstructure; mechanical property

Shape memory alloys (SMAs) are a class of smart materials capable of undergoing phase transformation from low-temperature martensite to high-temperature austenite through the thermodynamic mechanism of solid-state phase transformation, thereby restoring their preset shape via stress or temperature variations<sup>[1-3]</sup>. In recent years, the rapid advancement of industrial technology has escalated the performance requirements for functional materials. Particularly, in the field of SMAs, emerging industrial applications present new challenges and demands for innovation and high performance<sup>[4-7]</sup>. One of the principal constraints of traditional SMAs is their phase transition temperature, which restricts their application in high-temperature environments<sup>[8]</sup>. Over the past decade, significant

efforts have been dedicated to the high-temperature SMAs<sup>[9]</sup>. Currently, the most widely studied and promising material is Ni-Ti-based alloy<sup>[10]</sup>. In order to improve the phase transition temperature, noble metals such as Pd, Pt and Au can be added to Ni-Ti alloy to obtain higher martensite transition temperature ( $M_s$ ), but the shape memory effect of these alloys in high-temperature environment is reduced. In addition, the increase in price and demand of high-cost elements has significantly increased the manufacturing cost of the alloy<sup>[11-12]</sup>. In contrast, the phase transition temperature can be adjusted by replacing Ti or Ni with Hf or Zr in Ni-Ti alloys. Although the adjustment range is limited, the preparation cost of the alloy is low. Some alloys with specific composition ratios exhibit good thermal processing properties and have the

Received date: August 11, 2024

Foundation item: National Natural Science Foundation of China (12404230, 52061027); Science and Technology Program Project of Gansu Province (22YF7GA155); Lanzhou Youth Science and Technology Talent Innovation Project (2023-QN-91); Zhejiang Provincial Natural Science Foundation of China (LY23E010002)

Corresponding author: Zhao Yanchun, Ph. D., Professor, State Key Laboratory of Advanced Processing and Recycling of Nonferrous Metals, Lanzhou 730050, P. R. China, E-mail: zhaoyanchun@edu.lut.cn

Copyright © 2025, Northwest Institute for Nonferrous Metal Research. Published by Science Press. All rights reserved.

potential to replace precious metals such as Pd, Pt and Au in commercial applications<sup>[13]</sup>. Studies have shown that<sup>[14]</sup> although the addition of Zr or Hf may slightly increase the brittleness of the alloy, increasing Zr content causes a small changes in phase transition temperature, and Hf has a more significant effect. For instance, Bigelow et al<sup>[13]</sup> discovered that when the Zr content exceeds 10at%, the  $M_s$  increases significantly, with a rate of approximately 18 °C/1at%. Furthermore, studies have shown that<sup>[15-16]</sup> in the Ni-Ti-Hf ternary alloy, the phase transition temperature increases once the Hf content reaches 3at%; when the Hf content is 5at%–10at%, the increase rate is approximately 18 °C/1at%; when the Hf content exceeds 10at%, the increase rate is around 20 °C/1at%. Although Ni-Ti-Hf high-temperature SMAs exhibit good superelasticity and shape memory effects, their cycle stability, thermo-mechanical machinability and fatigue resistance are relatively poor. Therefore, further research is needed to enhance the application of high-temperature Ni-Ti-Hf SMAs.

As a new class of materials, high-entropy alloys have garnered significant attention from researchers because of their exceptional thermal stability and excellent mechanical properties. Among them, the most extensively studied alloy is the CoCrFeMnNi high-entropy alloy, which has a face-centered cubic (fcc) crystal structure and exhibits excellent mechanical properties at various temperatures<sup>[17-18]</sup>. However, compared to traditional alloys, achieving the simultaneous enhancement in both strength and plasticity of high-entropy alloys remains a challenge to be addressed. In 2015, Firstov et al<sup>[8,19]</sup> successfully integrated the concepts of high-entropy alloys and SMAs to design the (TiZrHf)<sub>50</sub>(NiCuCo)<sub>50</sub> series of high-entropy SMAs, yielding promising research outcomes. The findings indicate that replacing Ni and Cu with Co gradually decreases the martensitic transformation temperature of the (TiZrHf)<sub>50</sub>(NiCuCo)<sub>50</sub> series high-entropy SMAs, while the stability of austenite gradually increases. In the three-point bending test, the (TiZrHf)<sub>50</sub>Ni<sub>25</sub>Cu<sub>15</sub>Co<sub>10</sub> high-entropy SMA demonstrates a notable shape memory effect, with a recoverable strain of 1.63% under constant stress. Additionally, Chen et al<sup>[20]</sup> significantly enhanced the shape memory effect of the (TiZrHf)<sub>50</sub>Ni<sub>25</sub>Cu<sub>15</sub>Co<sub>10</sub> high-entropy SMA through heat treatment at 1273 K for 2 h, obtaining a recoverable strain of 4.8% in the three-point bending test. Currently, research on high-entropy SMAs is highly dispersed, and there is a lack of systematic and in-depth understanding of the phase transformation mechanisms of these alloys, which hinders the proposal of effective alloy design criteria and significantly impedes the design and development of high-performance high-entropy SMAs. Based on this, (TiZrHf)<sub>50</sub>Ni<sub>30</sub>Cu<sub>20-x</sub>Co<sub>x</sub> ( $x=2, 4, 6, \text{at}\%$ ) alloy samples were designed for the high-entropy SMA system. By adjusting the content of Cu and Co elements, the phase transformation behavior, mechanical properties and superelasticity of the alloy were studied. This research provides an experimental and theoretical basis for expanding the application range of high-entropy alloys and designing new high-performance, high-

temperature SMAs.

## 1 Experiment

(TiZrHf)<sub>50</sub>Ni<sub>30</sub>Cu<sub>20-x</sub>Co<sub>x</sub> ( $x=2, 4, 6, \text{at}\%$ ) high-entropy SMA samples with varying compositions were prepared using Ti, Zr, Hf, Ni, Cu and Co particles with a purity greater than 99.99wt%. Water-cooled copper crucible magnetic levitation melting and copper mold negative pressure suction casting techniques were used. The phase transition temperature of the alloy was analyzed by German-Nonch-DSC214 differential scanning calorimeter (DSC). The phase composition of the alloy was analyzed by X-ray diffractometer (XRD, D8ADVANCE type) and electron backscatter diffraction (EBSD) technique. The microstructure and element distribution of the alloy were analyzed by field emission scanning electron microscope (SEM, QUANTA FEG 450) and energy dispersive spectrometer (EDS). A universal mechanical testing machine (WDW-100 D type) was used with a test force of 50 kN and a displacement speed of  $5 \times 10^{-4}$  mm/s to screen alloys with excellent mechanical properties in quasi-static compression experiments. Subsequently, cyclic compression experiments were conducted to obtain relevant data such as superelastic recovery and irreversible strain.

## 2 Results and Discussion

### 2.1 Phase transformation behavior of alloys

Fig. 1 shows the DSC curves of the (TiZrHf)<sub>50</sub>Ni<sub>30</sub>Cu<sub>14</sub>Co<sub>6</sub> high-entropy high-temperature SMA, clearly indicating the start temperature of martensite transformation ( $M_s$ ), the finishing temperatures of martensite transformation ( $M_f$ ), the start temperature of austenite transformation ( $A_s$ ) and the finishing temperatures of austenite transformation ( $A_f$ ). The  $M_s$  temperature of the alloy exceeds 373 K (100 °C), consistent with the characteristics of high-temperature SMAs. During the heating and cooling processes, the DSC curve shows distinct endothermic and exothermic peaks, representing austenite and martensite phase transformations, respectively. The martensitic and austenitic phase transformation start temperatures of the (TiZrHf)<sub>50</sub>Ni<sub>30</sub>Cu<sub>14</sub>Co<sub>6</sub> alloy are 450.79 and 395.76 K, respectively, with termination

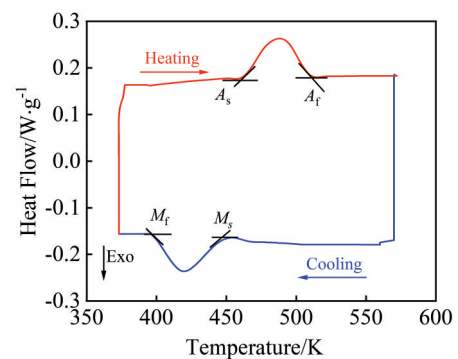


Fig.1 DSC curves of (TiZrHf)<sub>50</sub>Ni<sub>30</sub>Cu<sub>14</sub>Co<sub>6</sub> high-temperature high-entropy SMA

temperatures of 460.16 and 512.27 K, respectively. The thermal hysteresis ( $A_f - M_s$ ) is 61.48 K, the phase transformation interval ( $A_f - A_s$ ) is 52.11 K, and  $M_s - M_f$  is 55.03 K, indicating that the alloy exhibits significant thermal hysteresis and relatively wide phase transition temperature range. These characteristics are partly due to the special dendritic microstructure of the alloy, which causes differences in phase transition behavior between intergranular and intragranular regions. The phase transition temperature obtained from the DSC test reflects the average value of these regions. Additionally, it is due to the low geometric compatibility between austenite and martensite. These factors together cause the  $(\text{TiZrHf})_{50}\text{Ni}_{30}\text{Cu}_{14}\text{Co}_6$  alloy to exhibit large thermal hysteresis and wide phase transition range.

## 2.2 Microstructure of alloys

Fig. 2 shows the XRD patterns of as-cast and fractured  $(\text{TiZrHf})_{50}\text{Ni}_{30}\text{Cu}_{20-x}\text{Co}_x$  high-temperature high-entropy SMAs. From Fig. 2a, it can be observed that the alloy consists of austenite phase (B2) and martensite phase (B19') in the as-cast state. Changing the content of Cu and Co elements does not alter the phase composition of the matrix, because the atomic radii of Cu and Co are not significantly different, having little effect on the lattice constant. With the increase in Co content, the diffraction peak intensity of the B2 phase gradually increases. As seen in Fig. 2b, the alloy after fracture still consists of the B2 phase and the B19' phase, but the content of the B2 phase decreases significantly, and the content of the B19' phase increases. This is because during the post-fracture compression process, as the strain increases, the dislocation density in the B2 phase increases, slip deformation increases, and slip intersections provide nucleation sites for the

martensitic transformation. Once the stress reaches the critical level at which martensitic nucleation occurs, stress-induced martensitic transformation occurs, increasing the content of the B19' martensitic phase.

Fig. 3a – 3c shows the microstructure of  $(\text{TiZrHf})_{50}\text{Ni}_{30}\text{Cu}_{20-x}\text{Co}_x$  high-entropy alloys. The microstructure of this high-temperature SMA is similar to that of most as-cast high-entropy alloys, exhibiting a typical dendritic structure. Fig. 3d–3i shows the elemental analysis of  $(\text{TiZrHf})_{50}\text{Ni}_{30}\text{Cu}_{14}\text{Co}_6$  alloy. The results indicate that the elements in the alloy are evenly distributed without segregation. In general, high-entropy alloys with this microstructure exhibit high yield strength in high-temperature environment, because the hysteresis diffusion effect in the alloy can effectively inhibit crystal growth and facilitate microstructure nanocrystallization. Additionally, the lattice distortion caused by atoms of different sizes in high-entropy alloys significantly enhances the solid solution strengthening effect. Therefore, this high-entropy high-temperature SMA may exhibit high strength characteristics and high-temperature phase stability.

## 2.3 Compressive mechanical properties of alloys

Fig. 4 presents the stress-strain curves of  $(\text{TiZrHf})_{50}\text{Ni}_{30}\text{Cu}_{20-x}\text{Co}_x$  alloys with different sizes ( $d=2, 4, 6$  mm). At the same loading rate, the compressive strength ( $\sigma_f$ ) and plasticity ( $\sigma_p$ ) of the alloy slightly decrease with the increase in sample size. However, it can be observed that the effect of sample size on plasticity and yield strength ( $\sigma_y$ ) is not obvious. This is attributed to the lattice distortion effect and multi-element composition in the high-entropy alloy, which hinder dislocation movement and increase the slip systems. Consequently, the strength and plasticity of the alloy are enhanced, overcoming the partial size effect. Additionally, with increasing the Co content and decreasing the sample size, the grain size of the alloy is refined, which enhances the comprehensive mechanical properties of the alloy.  $(\text{TiZrHf})_{50}\text{Ni}_{30}\text{Cu}_{14}\text{Co}_6$  exhibits the best mechanical properties when  $d=2$  mm, with a compressive strength and plasticity of 2142.39 MPa and 17.31%, respectively. Table 1 shows the results of compressive mechanical properties of the alloy.

The results of Fig. 4 show that at the same loading rate, despite different sample sizes, these samples undergo a deformation process similar to that of the  $\text{Ti}_{69}\text{Zr}_{30}\text{Fe}_1$  high-temperature SMA studied by Zhang et al<sup>[21]</sup>. This process can be divided into two main stages: the first stage is the initial elastic deformation stage, which continues to about 7% strain. During this stage, the martensitic phase undergoes elastic deformation, and the critical stress is about 700 MPa, marking the beginning of the reorientation of martensitic twins. The second stage extends from 7% strain to failure, during which the “stress platform” typically observed in SMAs is absent, instead showing a feature similar to work hardening. This phenomenon is similar to the deformation characteristics of some high-temperature SMAs, mainly due to the irreversible deformation caused by dislocation slip while the martensite twins are reoriented.

Fig. 5 shows the fracture morphology of  $(\text{TiZrHf})_{50}\text{Ni}_{30}$

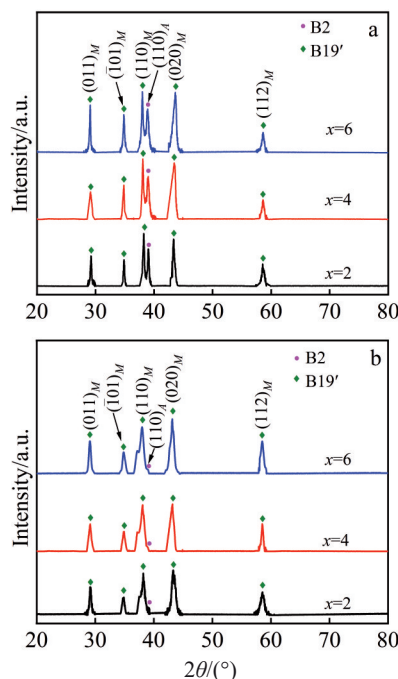


Fig.2 XRD patterns of  $(\text{TiZrHf})_{50}\text{Ni}_{30}\text{Cu}_{20-x}\text{Co}_x$  ( $x=2, 4, 6$ , at%) alloys: (a) as-cast and (b) post-fracture (subscript  $M$  and  $A$  refer to martensite and austenite, respectively)

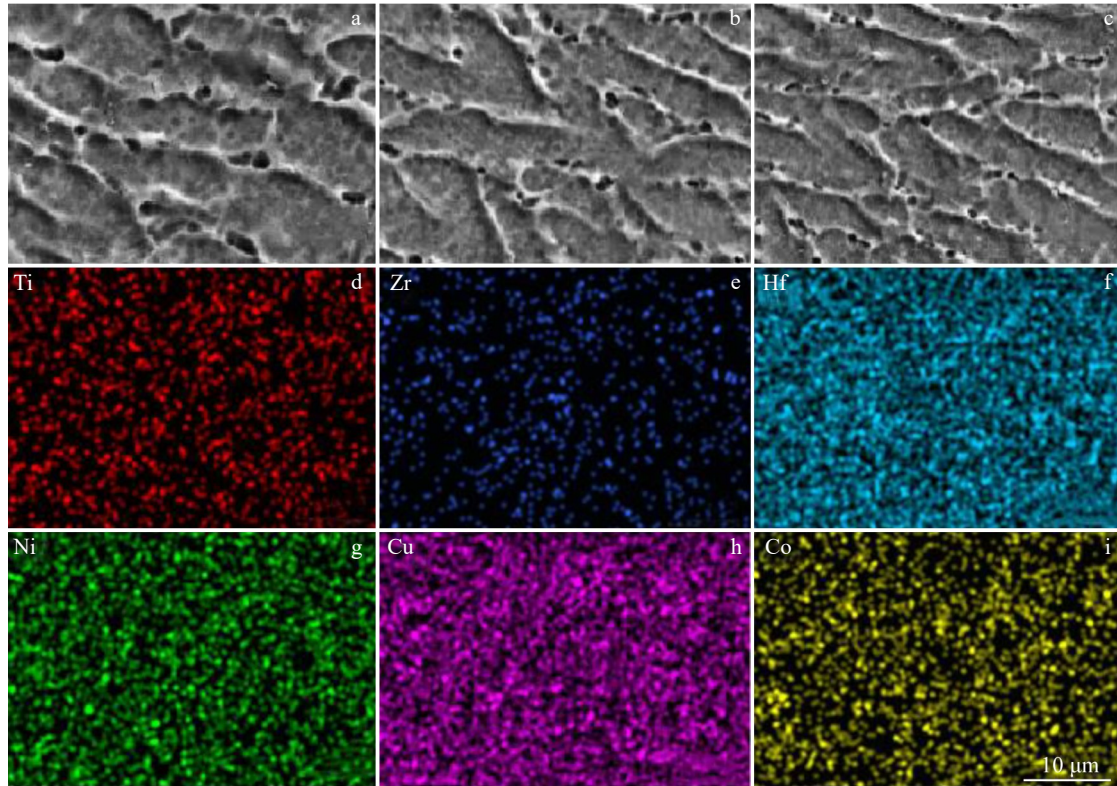


Fig.3 SEM microstructures of  $(\text{TiZrHf})_{50}\text{Ni}_{30}\text{Cu}_{20-x}\text{Co}_x$  alloys: (a)  $x=2$ , (b)  $x=4$ , and (c)  $x=6$ ; EDS mappings of element Ti (d), Zr (e), Hf (f), Ni (g), Cu (h), and Co (i) in  $(\text{TiZrHf})_{50}\text{Ni}_{30}\text{Cu}_{14}\text{Co}_6$  alloy

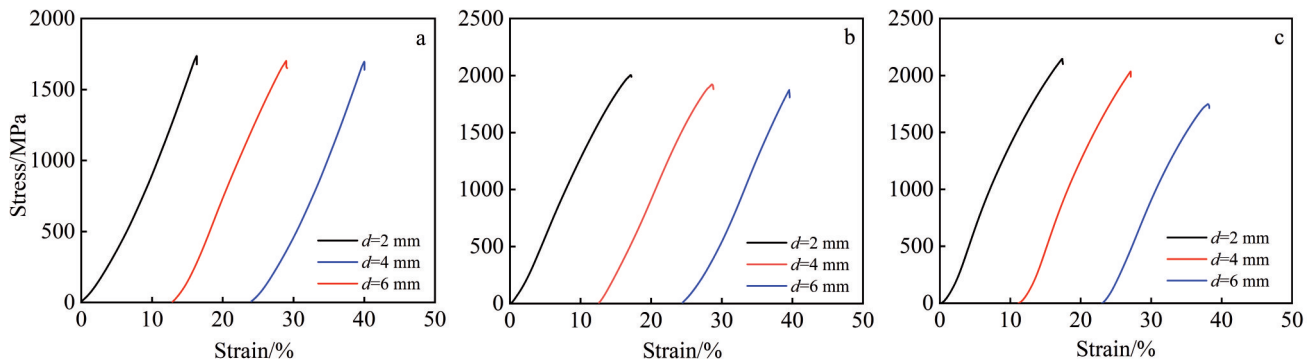


Fig.4 Engineering stress-strain curves of as-cast  $(\text{TiZrHf})_{50}\text{Ni}_{30}\text{Cu}_{20-x}\text{Co}_x$  alloys: (a)  $x=2$ , (b)  $x=4$ , and (c)  $x=6$

**Table 1** Compressive mechanical properties of  $(\text{TiZrHf})_{50}\text{Ni}_{30}\text{Cu}_{20-x}\text{Co}_x$  alloys with different sizes

$x$	Diameter, $d/\text{mm}$	$\sigma_s/\text{MPa}$	$\sigma_f/\text{MPa}$	$\varepsilon_p/\%$
2	2	734.07±2.1	1736.23±1.4	16.31±0.4
	4	727.62±1.7	1702.01±1.7	16.13±0.6
	6	719.98±1.4	1696.29±2.1	15.99±0.3
4	2	791.91±1.3	2003.82±1.4	16.91±0.4
	4	782.17±2.3	1923.30±1.5	15.99±0.3
	6	774.36±1.5	1873.65±1.3	15.10±0.4
6	2	846.84±1.8	2142.39±1.8	17.31±0.3
	4	826.73±2.4	2035.82±2.3	15.92±0.4
	6	814.61±1.6	1748.50±1.3	15.01±0.2

$\text{Cu}_{20-x}\text{Co}_x$  alloys. It can be observed that the fractures of these alloys exhibit river patterns and cleavage characteristics. With the increase in Co content, the cleavage fracture characteristics gradually decrease, corresponding to the increase in plasticity observed in the engineering stress-strain curve.

#### 2.4 Superelasticity of alloys

Based on the previous research, the  $(\text{TiZrHf})_{50}\text{Ni}_{30}\text{Cu}_{14}\text{Co}_6$  alloy with excellent mechanical properties at room temperature was selected to carry out the superelastic test with increasing the compressive strain. The applied compressive strains were 7%, 9%, 11%, 13% and 5%. The compression cycle curves of the  $(\text{TiZrHf})_{50}\text{Ni}_{30}\text{Cu}_{14}\text{Co}_6$  alloy are shown in Fig.6.

These curves demonstrate significant superelastic characteristics. The coincidence degree of curves under different

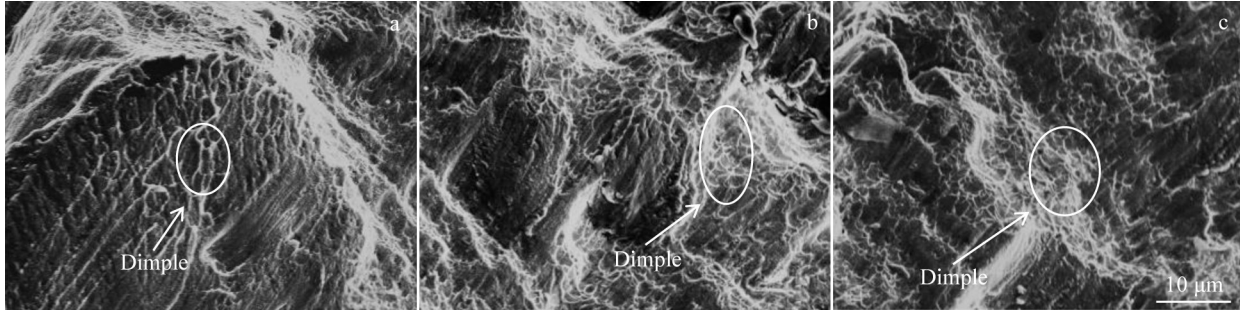


Fig.5 Fracture morphologies of  $(\text{TiZrHf})_{50}\text{Ni}_{30}\text{Cu}_{20-x}\text{Co}_x$  high-entropy alloys: (a)  $x=2$ , (b)  $x=4$ , and (c)  $x=6$

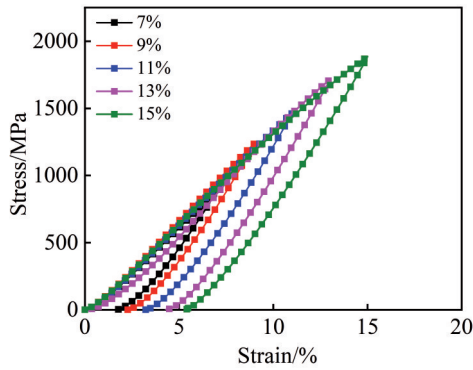


Fig.6 Compression cycle curves of as-cast  $(\text{TiZrHf})_{50}\text{Ni}_{30}\text{Cu}_{14}\text{Co}_6$  high-entropy alloy

compressive strains during the loading stage is very high, indicating stable superelastic behavior under various cyclic strains. As the compressive strain increases, the slope of the stress-strain curve gradually decreases during the unloading stage, and the area of the hysteresis loop gradually increases, indicating enhanced dissipation capacity. The increase in compressive strain leads to a more thorough martensitic transformation, and the content of the martensitic phase increases during the unloading stage. According to the calculation method in Fig.7, the recovery rate ( $\eta$ ), recoverable strain ( $\epsilon_r$ ), residual strain ( $\epsilon_l$ ), elastic recovery strain ( $\epsilon_E$ ), and superelastic recovery strain ( $\epsilon_{SE}$ ) are calculated from the compression cycle curves. The results are shown in Table 2.

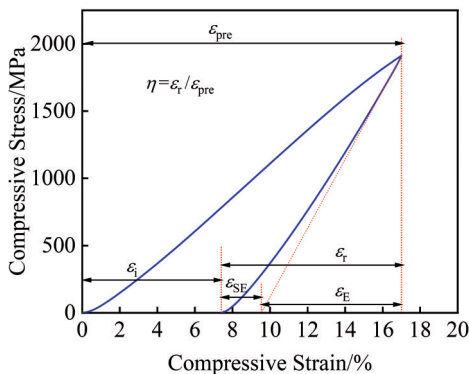


Fig.7 Schematic diagram of parameter calculation<sup>[22]</sup>

Table 2 Calculation results of parameters

$\epsilon_{pre}/\%$	$\eta/\%$	$\epsilon_l/\%$	$\epsilon_r/\%$	$\epsilon_E/\%$	$\epsilon_{SE}/\%$
7	74.48	5.21	1.79	3.86	1.36
9	73.07	6.58	2.42	4.97	1.60
11	69.95	7.69	3.31	5.78	1.92
13	66.46	8.64	4.36	6.59	2.06
15	63.20	9.48	5.52	7.36	2.12

It can be seen from Fig.7 that as the compressive strain increases, the residual strain accumulated in the alloy increases, resulting in a decrease in the recovery ability of the alloy. At the same time, the recoverable strain, elastic recovery strain and superelastic recovery strain of the alloy increase as the compressive strain increases, but the growth rate gradually slows down. In the early stage of stress-induced martensitic transformation, the content of stress-induced martensite phase increases rapidly, resulting in a fast growth rate of elastic recovery. In the later stage of stress-induced martensitic transformation, the content of the martensite phase decreases, leading to a decrease in the increase rate of elastic recovery. As the compressive strain increases, the superelastic recoverable strain can increase from 1.36% to 2.12%, the residual strain increases from 1.79% to 5.52%, the elastic recovery increases from 3.86% to 7.36%, and the recovery rate decreases from 74.48% to 63.20%. In the initial stage, when the compressive strain is small, the recoverable strain of the alloy is mainly achieved through elastic deformation, which has a high recovery rate. As the compressive strain continues to increase, stress-induced martensitic transformation increases, and thus superelastic recovery occupies a larger proportion of the total recoverable strain. However, with further increase in compressive strain, on the one hand, some martensite phases undergo irreversible plastic deformation; on the other hand, plastic deformation and dislocation accumulation hinder the reverse phase transformation of martensite, resulting in stabilization of some martensite phases. These two factors work together, eventually leading to a downward trend in the growth rate of the superelastic recovery strain of the alloy.

## 2.5 Phase composition analysis based on EBSD

To further study the phase composition of  $(\text{TiZrHf})_{50}\text{Ni}_{30}\text{Cu}_{20-x}\text{Co}_x$  high-entropy SMAs, the  $(\text{TiZrHf})_{50}\text{Ni}_{30}\text{Cu}_{14}\text{Co}_6$  alloy

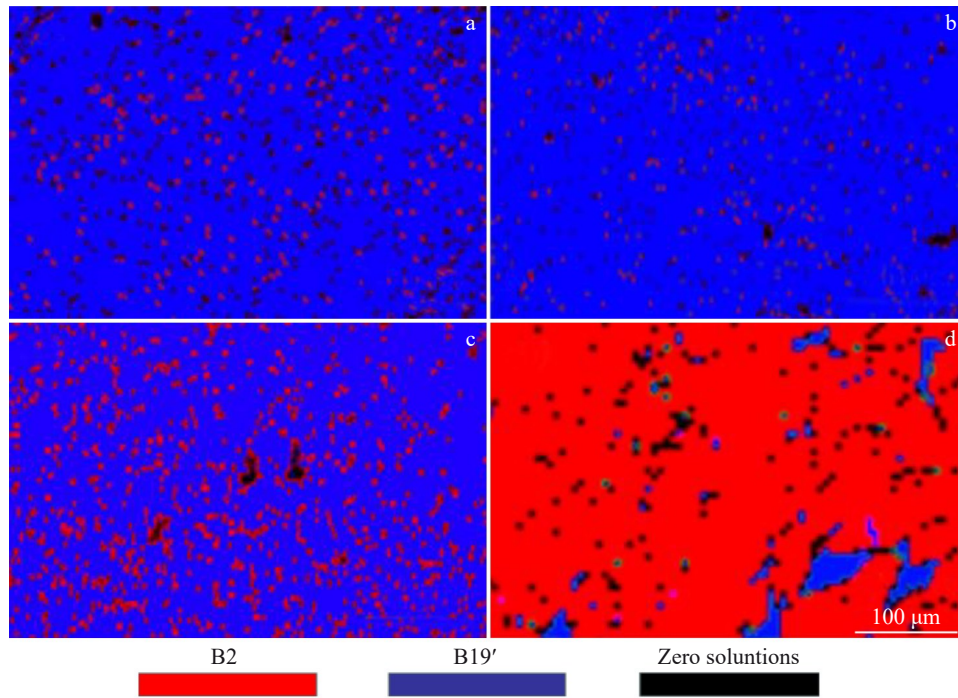


Fig.8 EBSD patterns of  $(\text{TiZrHf})_{50}\text{Ni}_{30}\text{Cu}_{14}\text{Co}_6$  high-entropy alloy: (a) as-cast; (b) post-fracture; (c) heat treatment for 30 min; (d) heat treatment for 1 h

was heat treated at 350 °C for 30 min and 1 h above the  $A_f$  phase transition temperature. EBSD was used to analyze the content changes of as-cast and heat-treated samples. Before testing, samples with intact surface structures were selected to avoid the influence of holes or cracks on subsequent electrolytic polishing and EBSD detection. The sample was firstly mechanically polished along the direction of force and then electropolished in the electrolyte for about 20 s. Finally, the polished sample was dried for EBSD analysis.

As shown in Fig.8, the phase distribution of the  $(\text{TiZrHf})_{50}\text{Ni}_{30}\text{Cu}_{14}\text{Co}_6$  SMA under different conditions is presented. The as-cast alloy exhibits only a small number of B2 austenite phase and B19' martensite phase, which is consistent with the XRD results. The content of the B2 phase decreases after fracture, indicating that stress-induced martensitic transformation ( $\text{B2} \rightarrow \text{B19}'$ ) occurs during the compression process. The newly formed B19' phase is mainly located in the loading direction, which is in good agreement with the XRD test results.

Additionally, under heat treatment at 350 °C, part of the B19' phase is reversed to the B2 phase, indicating reversible recovery in the microstructure. The relative content of the B2 phase increases significantly as the heat treatment proceeds. According to the phase resolution rate shown in Table 3, with prolonging the heat treatment time, more B19 phases reverse to B2 phases, and the recovery rate significantly improves. However, the recovered structure fails to fully recover to the state before deformation. The new B19' martensite phase formed by stress induction has poor compatibility with the parent phase austenite, resulting in partial irreversible deformation. Therefore, the residual B19' martensite phase

Table 3 Phase analysis rate corresponding to EBSD pattern of  $(\text{TiZrHf})_{50}\text{Ni}_{30}\text{Cu}_{14}\text{Co}_6$  high-entropy alloy (%)

Sample	B2	B19'	Zero solutions
As-cast	7.9	85.8	6.3
Post-fracture	2.6	90.2	7.2
Heat treatment for 30 min	38.5	56.1	5.4
Heat treatment for 1 h	83.7	10.2	6.1

still exists in the alloy structure after heat treatment.

### 3 Conclusions

1) As the Co content increases in the  $(\text{TiZrHf})_{50}\text{Ni}_{30}\text{Cu}_{20-x}\text{Co}_x$  ( $x=2, 4, 6$ , at%) high-entropy SMAs, there is a significant diminution in grain size. In the as-cast state, the microstructure predominantly consists of B19' phase with a trace of B2 phase. Upon fracture, the microstructure is primarily characterized by the B19' martensite phase, while the B2 phase is virtually absent.

2) The compressive strength and plasticity of the  $(\text{TiZrHf})_{50}\text{Ni}_{30}\text{Cu}_{20-x}\text{Co}_x$  high-entropy SMAs are augmented with the rise in Co content and the diminution in sample size. When the diameter is 2 mm, the  $(\text{TiZrHf})_{50}\text{Ni}_{30}\text{Cu}_{14}\text{Co}_6$  alloy exhibits the most favorable comprehensive mechanical properties, boasting a compressive strength of  $2142.39 \pm 1.8$  MPa and a plastic strain of  $17.31 \pm 0.3\%$ .

3) In the compression cycle tests performed on the  $(\text{TiZrHf})_{50}\text{Ni}_{30}\text{Cu}_{14}\text{Co}_6$  alloy, an increase in compression strain leads to a rise in residual strain and a decline in recovery capacity. Although the recoverable strain escalates as the strain increases, the increase rate tapers off progressively.

Concurrently, the superelastic recovery of the alloy is enhanced, with the superelastic recovery rate escalating from 1.36% to 2.12%, the residual strain rate climbing from 1.79% to 5.52%, the elastic recovery rate ascending from 3.86% to 7.36%, and the total recovery rate diminishing from 74.48% to 63.20%.

## References

- 1 Yan Fei, Du Xinghao, Jin Chenyan et al. *Rare Metal Materials and Engineering*[J], 2023, 52(1): 179 (in Chinese)
- 2 Zhao Yanchun, Feng Yuanfei, Feng Li et al. *Rare Metal Materials and Engineering*[J], 2024, 53(3): 848 (in Chinese)
- 3 Easo P G, Dierk R, Robert O R. *Nature Reviews Materials*[J], 2019, 4(8): 515
- 4 Li Binqiang, Wang Liang, Yao Longhui et al. *Rare Metal Materials and Engineering*[J], 2021, 50(6): 2208 (in Chinese)
- 5 Zhao Y C, Song H Z, Ma H W et al. *Rare Metal Materials and Engineering*[J], 2024, 53(7): 1817
- 6 Ma H W, Zhao Y C, Feng L et al. *Rare Metals*[J], 2024, 43: 4496
- 7 Guo Wenhui, Qi Mingfan, Xu Yuzhao et al. *Rare Metal Materials and Engineering*[J], 2022, 51(7): 2570 (in Chinese)
- 8 Firstov G S, Kosorukova T A, Koval Y N et al. *Materials Today Proceedings*[J], 2015, 2(3): 499
- 9 Popov N N, Grishin E N, Syssoeva T I et al. *Inorganic Materials: Applied Research*[J], 2024, 15(1): 215
- 10 Massad J E, Buchheit T E, Susan D F et al. *Journal of Intelligent Material Systems and Structures*[J], 2023, 34(4): 393
- 11 Shuitcev A, Li Q, Khomutov M et al. *Journal of Materials Science & Technology*[J], 2024, 209: 124
- 12 Ramaiah K V, Saikrishna C N, Bhaumik S K. *Materials Characterization*[J], 2015, 106: 36
- 13 Bigelow G S, Benafan O. *Scripta Materialia*[J], 2021, 194: 113623
- 14 Karakoc O, Hayrettin C, Bass M et al. *Acta Materialia*[J], 2017, 138: 185
- 15 Santamarta R, Arróyave R, Pons J et al. *Acta Materialia*[J], 2013, 61(16): 6191
- 16 Baradari S, Resnina N, Belyaev S et al. *Advanced Engineering Materials*[J], 2022, 24(10): 2200106
- 17 Wu W Q, Zhang L, Qiao J C et al. *Journal of Materials Science & Technology*[J], 2023, 153: 242
- 18 Li H G, Che P C, Yang X K et al. *Rare Metals*[J], 2022, 41(4): 1210
- 19 Firstov G S, Van H J, Koval Y N. *Journal of Intelligent Material Systems and Structures*[J], 2006, 17(12): 1041
- 20 Chen C H, Chen Y J. *Scripta Materialia*[J], 2019, 162: 182
- 21 Zhang Fei, Cui Yan, Xue Pengfei et al. *Rare Metal Materials and Engineering*[J], 2013, 42(10): 2131 (in Chinese)
- 22 Du F, Deng L, Zhang M et al. *Materials Today Communications*[J], 2024, 39: 109353

## Co含量对高熵高温形状记忆合金的组织及力学性能影响

赵燕春<sup>1,2</sup>, 金博<sup>1</sup>, 冯远飞<sup>1</sup>, 马虎文<sup>1</sup>, 于志琦<sup>1</sup>, 冯力<sup>1,2</sup>, Liaw Peter K<sup>3</sup>

(1. 兰州理工大学 省部共建有色金属加工与再利用国家重点实验室, 甘肃 兰州 730050)

(2. 兰州理工大学温州泵阀工程研究院, 浙江 温州 325105)

(3. 田纳西大学 材料系, 美国 诺克斯维尔 TN37996)

**摘要:** 采用水冷铜坩埚磁悬浮真空熔炼炉制备了(TiZrHf)<sub>50</sub>Ni<sub>30</sub>Cu<sub>20-x</sub>Co<sub>x</sub>(x=2, 4, 6, at%)高熵高温形状记忆合金, 并研究了Co含量对其微观组织和力学性能的影响。结果表明, 随着Co含量增加, 合金晶粒尺寸减小。合金在铸态下主要由B19'和少量B2相组成, 断口组织富含B19'相, 而B2相几乎消失。增加Co含量和缩小试样尺寸(*d*)显著提升了合金的抗压强度和塑性, 在*d*=2 mm时, (TiZrHf)<sub>50</sub>-Ni<sub>30</sub>Cu<sub>14</sub>Co<sub>6</sub>合金表现出最佳综合力学性能, 抗压强度为2142.39±1.8 MPa, 塑性为17.31±0.3%。压缩循环试验显示, 随着压缩应变增加, (TiZrHf)<sub>50</sub>Ni<sub>30</sub>Cu<sub>14</sub>Co<sub>6</sub>合金的残余应变增大, 但回复能力减弱。合金的超弹性回复能力不断增强, 超弹性回复率从1.36%增至2.12%, 残余应变率从1.79%增至5.52%, 弹性回复率从3.86%增至7.36%, 总回复率从74.48%降至63.20%。

**关键词:** 高温形状记忆合金; 高熵合金; 微观组织; 力学性能

**作者简介:** 赵燕春, 女, 1984年生, 博士, 教授, 兰州理工大学省部共建有色金属先进加工与再利用国家重点实验室, 甘肃 兰州 730050, E-mail: zhaoyanchun@edu.lut.cn